A&A 416, 333–340 (2004)
DOI: 10.1051/0004-6361:20035636

Astronomy & Astrophysics

DOT tomography of the solar atmosphere

II. Reversed granulation in Ca II H

R. J. Rutten[1,2], A. G. de Wijn[1], and P. Sütterlin[1]

[1] Sterrekundig Instituut, Utrecht University, Postbus 80 000, 3508 TA Utrecht, The Netherlands
e-mail: [R.J.Rutten; A.G.deWijn; P.Suetterlin]@astro.uu.nl
[2] Institute of Theoretical Astrophysics, Oslo University, PO Box 1029 Blindern, 0315 Oslo, Norway

Received 5 November 2003 / Accepted 28 November 2003

Abstract. High-quality simultaneous image sequences from the Dutch Open Telescope (DOT) in the G band and the Ca II H line are used to quantify the occurrence of reversed granulation as a constituent of the subsonic brightness pattern observed as a background to acoustic oscillations in the quiet-Sun internetwork atmosphere. In the middle photosphere reversed granulation constitutes a much larger part of this background than at the larger heights sampled by ultraviolet radiation. The anticorrelation with the underlying granulation reaches about 50% at a temporal delay of 2–3 min, and increases with spatial image smoothing to mesogranular resolution. We discuss the nature of reversed granulation in terms of convection reversal, gravity waves, acoustic waves, and intergranular magnetism, suggest that the internetwork background pattern is primarily a mixture of the first two ingredients, and speculate that it is also an inverse canopy mapper.

Key words. Sun: photosphere – Sun: chromosphere – Sun: oscillations

1. Introduction

We use dual-wavelength observations from the Dutch Open Telescope (DOT, Rutten et al. 2004) to study "reversed granulation" observed in the middle solar photosphere. Our analysis follows on and is complementary to the ultraviolet probing of somewhat higher layers in the quiet solar atmosphere by Rutten & Krijger (2003; henceforth Paper I), who studied simultaneous 1600 Å, 1700 Å and white-light image sequences from TRACE (Handy et al. 1999) and concluded that the slowly varying meso-scale brightness pattern observed in the ultraviolet from quiet-sun internetwork areas is dominated by atmospheric gravity waves. Part of this identification consisted of demonstrating that reversed granulation plays only a minor role in shaping the ultraviolet background pattern. The pertinent literature on atmospheric gravity waves and reversed granulation was summarized in the introduction of Paper I. More recent work is discussed in Sect. 4 below.

In this paper we use simultaneous Ca II H and G-band imaging to study the internetwork background pattern deeper down in the solar atmosphere and at higher angular resolution. Reversed granulation appears to be a more important ingredient at these lower heights. We quantify its role using similar techniques as in Paper I, and we discuss its nature.

Send offprint requests to: R. J. Rutten,
e-mail: R.J.Rutten@astro.uu.nl

Since the figures below share the format of those in Paper I but differ significantly, we invite the reader to have a copy of Paper I at hand for comparison. Additional discussion of the TRACE results is given in the second half of Rutten (2003).

2. Observations and reduction

On December 8, 2002 a tandem image sequence was obtained during UT 11:06–12:00 with the Dutch Open Telescope (DOT) at the Observatorio del Roque de los Muchachos on La Palma. The telescope was pointed at a very quiet area at disk center. The sequence consists of simultaneous speckle-restored images taken in the G band (4305 Å) and Ca II H (3968 Å) and is the first tomographic DOT sequence combining these two diagnostics. Details on the telescope and DOT tomographic multi-wavelength imaging, speckle acquisition, speckle reconstruction, and standard reduction procedures are given in Rutten et al. (2004). Sample images are shown in Fig. 1.

The G-band and Ca II H speckle bursts were taken synchronously at 30 s cadence. After speckle reconstruction, small magnetic features common to both diagnostics were used to correct for slight differences in the image scales and orientations. Each sequence was then self-aligned using Fourier correlation. Their temporal averages were used for final co-alignment and clipping to the common field of view (79×63 arcsec^2). Blinking the two resulting sequences shows that their cross-alignment is maintained to within the

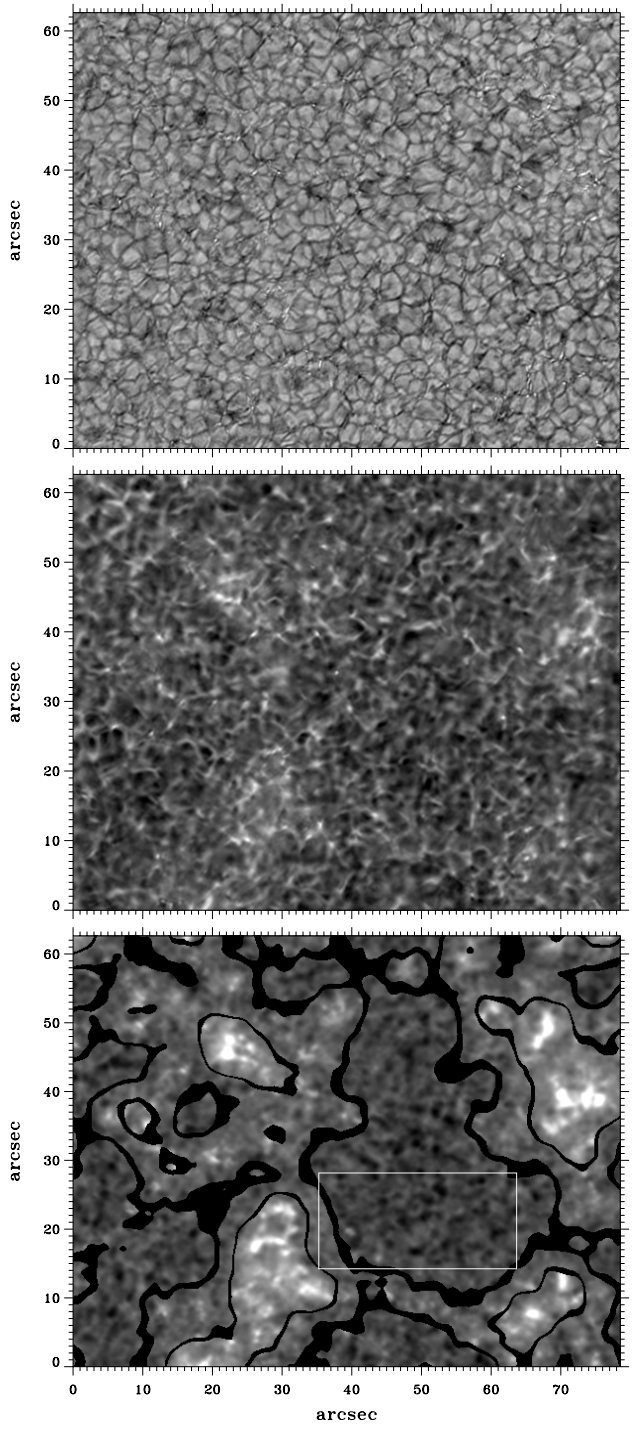

Fig. 1. *Top*: speckle-reconstructed G-band image (Nr. 1 of the sequence). The seeing during the speckle burst had Fried parameter $r_0 = 7$ cm. *Middle*: simultaneous Ca II H image, $r_0 = 6$ cm. *Bottom*: temporal mean of the Ca II H images with the network, intermediate, and internetwork mask borders overlaid. The network is overexposed to enhance internetwork visibility. The box specifies the subfield used in Fig. 2.

resolution. They are available as MPEG movie at the DOT website[1] and as FITS files from the authors.

[1] `http://dot.astro.uu.nl`

The seeing was only fair, with the Fried parameter r_0 varying between 5 and 8 cm between bursts (Fig. 3 of Rutten et al. 2004), but the image quality after speckle reconstruction of even the worst bursts still permits the precise mapping of granules and intergranular lanes needed for this analysis. The presence of many G-band bright points underlying chromospheric Ca II H network indicates angular resolution beyond 0.5 arcsec (cf. Title & Berger 1996). A particularly important advantage of the speckle processing is the resulting homogeneity over the full field of view and the full duration. The Ca II H image sequence is much better than any other Ca II H or K sequence we have analyzed or inspected so far (e.g., Hoekzema & Rutten 1998; Lites et al. 1999; Hoekzema et al. 2002).

The bottom panel of Fig. 1 shows the 53 min temporal average of all Ca II H images, together with spatial masks constructed from this image after spatial smoothing. They divide the field of view into network, intermediate, and internetwork pixels according to their mean Ca II H brightness. Some pixels are excluded from all three (black). The intermediate brightness category is likely to mark field spreading in low-lying "magnetic canopies" (cf. Krijger et al. 2001; McIntosh et al. 2003).

The exact wavelength position of the 1.35 Å wide Ca II H bandpass is not known since the filter was not yet mounted in its precisely tiltable holder. A small tilt causes violetward passband shift from line center. The appearance of the internetwork as a sharp "mesh" pattern with rather few acoustic grains suggests that the passband was shifted somewhat into the inner wing, because Ca II H line-center filtergrams show oscillation grains more prominently even at such wide spectral bandpass (cf. the spectral integrations in Rutten 1994 and Rutten et al. 1999). The Ca II H images therefore sample the solar photosphere only a few hundred km above $\tau_{5000} = 1$, at roughly half the heights imaged in the ultraviolet passbands of TRACE which sample the temperature minimum region in terms of VAL3C modeling (Vernazza et al. 1981).

In some displays below three-dimensional spatio-temporal Fourier cone filtering is employed to either select or remove all brightness modulation components with apparent horizontal speeds above or below 7 km s^{-1}. The "supersonic" high-pass filter selects the acoustic p-mode and three-minute oscillations. The "subsonic" low-pass filter removes these. The filter cutoff is indicated in Figs. 6–7.

3. Analysis and results

Space-time presentations. Figure 2 compares spatial and temporal brightness patterns between G band and Ca II H for the small subfield outlined in the bottom panel of Fig. 1. The format is comparable to Fig. 1 of Paper I, but the angular resolution is three times higher.

The Ca II H sub-image in the top right panel shows typical internetwork background consisting of a mesh pattern with superimposed grains (Lites et al. 1999). The subfield contains no strong network, but a "persistent flasher" (Brandt et al. 1992, 1994) is present near $(x, y) = (39, 20)$ and shows up as bright point in the Ca II H image. It is identified as an isolated magnetic element by its bright trail in the low-pass time slices (third row, clearest in Ca II H at right). Both trails are cut off

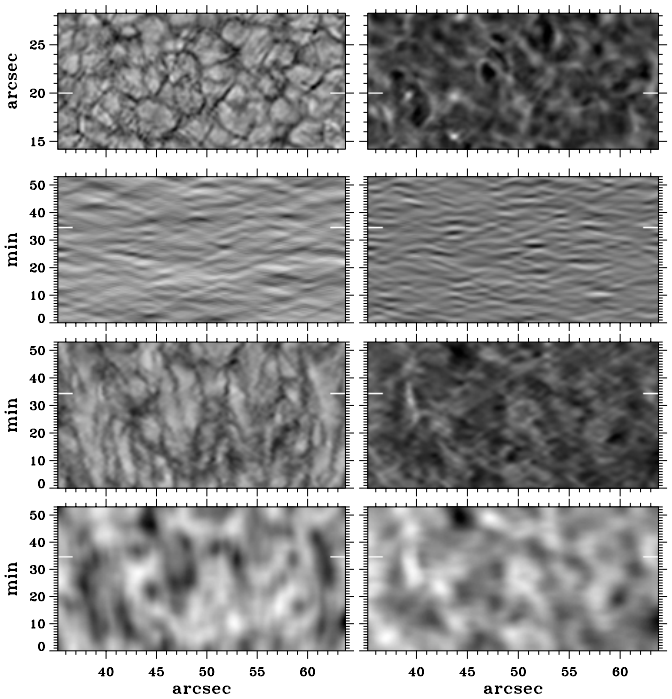

Fig. 2. Partial images and time slices for the subfield shown in the bottom panel of Fig. 1. *Left*: G band. *Right*: Ca II H. *First row*: brightness images. *Other rows*: time slices showing the brightness evolution along the horizontal cut defined by the white markers in the top-row images. The time-slice markers specify the time of observation of the image cutouts. *Second row*: supersonic brightness variations only. *Third row*: subsonic components only. *Bottom row*: subsonic time slices after 1.5 arcsec spatial smoothing, brightness rescaling, and brightness reversal for the G-band slice at left.

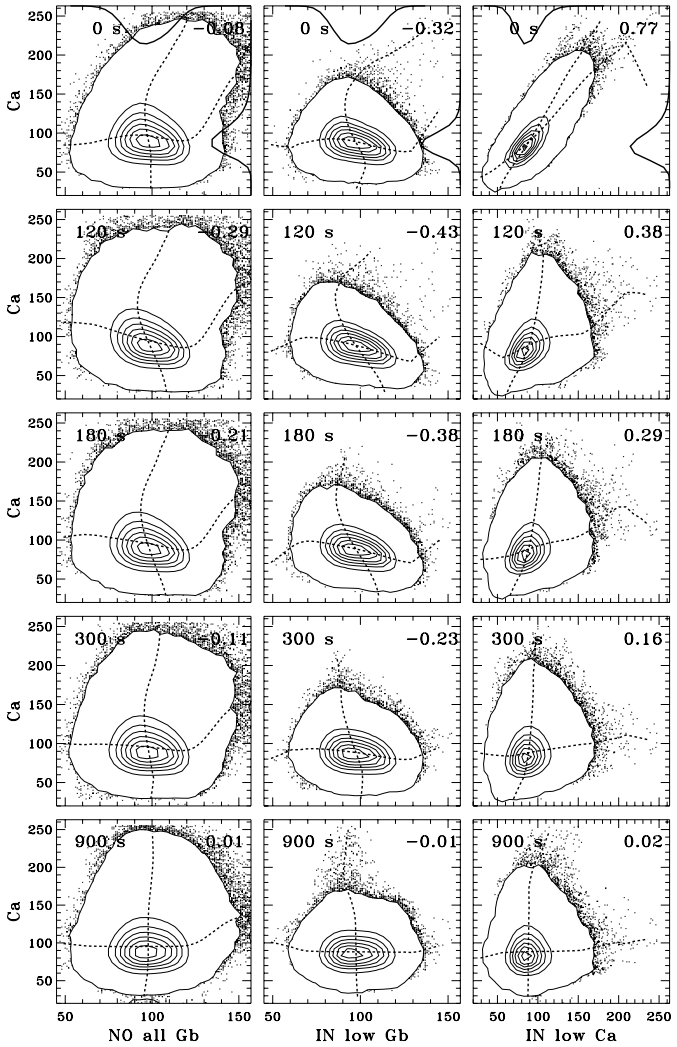

Fig. 3. Time-delay scatter correlations. *First column*: unfiltered Ca II H brightness Ca $(t + \Delta t)$ against unfiltered G-band brightness Gb (t) for the whole field. *Second column*: low-pass Ca $(t + \Delta t)$ against low-pass Gb (t) for internetwork pixels only. *Third column*: unfiltered Ca $(t + \Delta t)$ against low-pass Ca (t) for internetwork pixels only. Scales: brightness in arbitrary units. The time delay Δt is specified at left in each panel, the overall correlation coefficient at right. The solid curves in the top panels show the occurrence distributions on inverted normalized scales. The dashed curves show the first moments of the sample density distributions over x and y bins.

by feature motion in y; they extend over longer duration when one wiggles the y-location of the cut slightly using an interactive triple-plane cube slicer. The Ca II H grain is then seen to persist during the whole observing period. The bright grain near (44, 16) in the top-right image is similarly identifiable as the only other magnetic one in the subfield.

In contrast, the roundish Ca II H grain at (44, 20) is a regular acoustic "internetwork grain", appearing as a maximum in a three-minute oscillation wave train in the high-pass time slices (second row) without particular signature in the low-pass slices (third row). The grain near (44, 28) is also acoustic.

Summation of the low-pass and high-pass slices constitutes the total brightness evolution along the x cut. For both the G band and for Ca II H, most of the spatial pattern in the top-row images is due to subsonic brightness components, with superimposed acoustic modulations. For the G band, the subsonic evolution pattern corresponds to the granulation. For Ca II H, part of the subsonic pattern seems to be reverse granulation. This is illustrated by the bottom panels. These are also low-pass filtered time slices, but smoothed by 1.5 arcsec boxcar averaging to meso-scale resolution, each rescaled to the low-pass brightness contrast, and with the G-band brightness reversed to display literally reversed granulation. Comparison of the two bottom panels indicates coarse similarity, especially when admitting a few minutes delay for Ca II H and ignoring the magnetic grain. Such similarity lacks in the similar white light – ultraviolet time slice comparisons in Fig. 1 of Paper 1.

Time-delay correlations. Figure 3 presents pixel-by-pixel correlation diagrams similar to Fig. 2 of Paper I. Each panel is a scatter plot in which each sample specifies y-axis brightness versus x-axis brightness for a given pixel. Thirty successive image pairs are used to generate millions of samples. Plot saturation is avoided by showing sample density contours rather than individual points, except for the extreme outliers. The brightness distributions are shown in the top panels. The time delay Δt between x and y sampling (y after x) increases along columns as indicated. The dashed first-moment curves

are aligned at large correlation and become perpendicular in the absence of any correlation between the x and y quantities.

The first column of Fig. 3 shows Ca II H brightness (Ca) against G-band brightness (Gb) for the full unmasked field (NO) and without Fourier filtering (all). Network causes the lopsided high-intensity tail showing persistent bright-bright correlation. The main contour "mountain" is dominated by internetwork and shows some reversed bright-dark anticorrelation. This reversal is isolated in the second column which samples only the internetwork areas (IN) and the subsonic variations (low), for both Ca and Gb. The brightest Ca pixels are deleted through the removal of magnetic network grains and acoustic internetwork grains. The slight remaining initial bright-bright correlation is due to internetwork flashers. The contour mountain shows significant anticorrelation, peaking at $\Delta t = 2{-}3$ min delay. This is the signature of reversed granulation. It reaches overall correlation $C = -0.43$ in the second panel, twice as large as the corresponding UV–WL anticorrelation in Fig. 2 of Paper I.

The third column of Fig. 3 correlates unfiltered internetwork Ca with its own low-frequency components. The upward distribution tail describes internetwork grains. The very high initial bright-bright correlation confirms the finding from the similar third column of Fig. 2 of Paper I that most internetwork grains derive their excessive brightness from constructive addition of acoustic and low-frequency modulation peaks. At this height (where three-minute waves have not yet steepened into shocks) the average subsonic contribution is two-thirds of the excess grain brightness. The subsonic pattern is a much more ubiquitous grain co-localiser than "acoustic events" which cause only a few extreme ones (Hoekzema et al. 2002).

Figure 4 shows the temporal evolution of the overall correlation coefficient in various scatter comparisons. All curves are for internetwork low-pass variations only. The solid curves describe Gb–Gb and Ca–Ca autocorrelations, i.e., the persistence of surface granulation and of the non-acoustic Ca II H internetwork background pattern. The $1/e$ lifetimes are 4.5 min and 3.0 min, respectively.

The lower dashed curve shows the Ca–Gb crosscorrelation on a reversed scale and corresponds to the middle column of Fig. 3. After the initial rise it roughly mimicks the Gb–Gb pattern loss curve.

The upper dashed curve in Fig. 4 shows the Ca–Gb anticorrelation after 1.5 arcsec boxcar smoothing of all images, as for the TRACE data in Paper I and in the bottom panels of Fig. 1. The peak then comes a minute later and reaches $-C = 0.56$. Thus, reversed granulation describes a meso-scale reversal pattern that was already resolved in the TRACE data. At the Ca II H inner-wing formation height it has substantial but imperfect reversal signature compared with the spatially smoothed underlying granulation about three minutes earlier. The low corresponding UV–WL anticorrelation ($-C = 0.22$ at $\Delta t = 3{-}5$ min) in the middle column of Fig. 2 in Paper I implies intrinsic loss of this reversal signature with increasing height.

Fourier presentations. Figures 5–7 complete our data presentation through Fourier analysis corresponding to Figs. 4 and 5

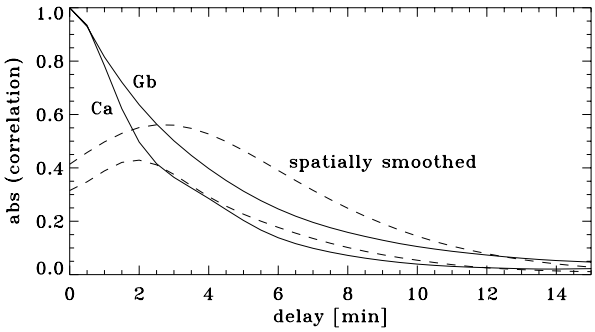

Fig. 4. Temporal evolution of pattern correlations, limited to internetwork areas and subsonic changes only. Solid: autocorrelations for G band (upper curve) and Ca II H (lower curve). Dashed: sign-reversed crosscorrelations between G band and Ca II H. The upper dashed curve results when the G band and Ca II H images are spatially smoothed to 1.5 arcsec resolution as for the TRACE data in Paper I.

of Paper I. The upper panel of Fig. 5 plots internetwork phase differences $\Delta\phi$ (Gb – Ca) in the format defined in detail by Krijger et al. (2001). The average is significant up to $f = 10$ mHz. The positive $\Delta\phi$ increase over $f = 5{-}10$ mHz describes the upward propagating acoustic waves modeled by Carlsson & Stein (1997). The zero crossing near five-minute periodicity describes evanescent p-mode behavior. The steep downturn at the lowest frequencies corresponds to the time-delayed anticorrelation in the second column of Fig. 3. The power spectra in the lower panel show that, even though acoustic power gains relative importance when going up from the G-band to Ca II H, the subsonic components dominate the Ca II H internetwork brightness pattern. The coherence is significant only in the propagating-wave and reversed-granulation domains.

Figure 6 decomposes the G-band and Ca II H brightness power measured over the whole field into temporal and spatial frequencies. These (k_h, f) diagrams mix network and internetwork properties, but the latter dominate due to the quietness of the observed region (Fig. 1). The lower-left region of interest here contains much power in both cases, with a shift to larger spatal scales for Ca II H. The acoustic domain illustrates the familiar shift from five-minute p-mode preponderance in the photosphere to three-minute oscillations higher in the atmosphere.

The upper panel of Fig. 7 decomposes the phase differences $\Delta\phi$ (Gb – Ca) in similar (k_h, f) format. This diagram is of much better quality than its noisy TRACE counterpart in Fig. 5 of Paper I, reaching much higher spatial wavenumbers before the noise (crowded contours) takes over.

Reversed granulation emerges as a large low-frequency patch of phase reversal stretching over $k_h = 1{-}5$ arcsec^{-1}. This patch extends to much higher wavenumber than the corresponding negative-phase patches in Figs. 3 and 5 of Paper I. (The wraparound evident at low frequency in Fig. 5 necessitated use of a greyscale that does not flip sign at $\Delta\phi = -180$ degrees. We suspect that phase wraparound causes apparently positive phase around $k_h = 3$ arsec^{-1} in Fig. 5 of Paper I). However, although this patch extends to $k_h = 5$ arcsec^{-1}, it is important to note that the power increases to larger scales for

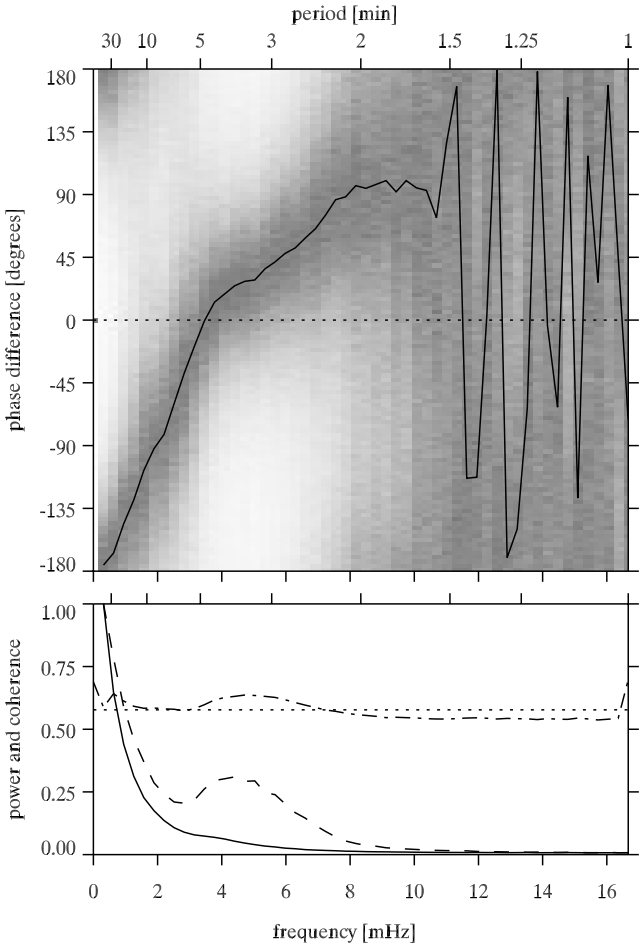

Fig. 5. G-band and Ca II H Fourier spectra, for internetwork only. *Upper panel*: phase differences $\Delta\phi$ (Gb – Ca) between G-band and Ca II H brightness. Grey scale: amplitude-weighted phase differences per pixel following the recipe of Krijger et al. (2001). The jagged fluctuations of the mean curve above $f = 10$ mHz indicates domination by noise. *Second panel*: corresponding power spectra (solid for Gb, dashed for Ca, mean and trend removed, normalized at the first non-zero frequency) and coherence spectrum with dashed noise estimate.

both G-band and Ca II H, and faster for the latter (lower panel of Fig. 7). The subsonic background to the Ca II H internetwork pattern is therefore dominated by mesogranular scales, and these set most of the anticorrelation making up reversed granulation.

Above the reversed-phase patch, the phase differences transit to the evanescent ($\Delta\phi = 0$) p-mode domain at small wave number and propagative ($\Delta\phi > 0$) three-minute domains. Significant $\Delta\phi/k_{\rm h}$ gradients occur up to $f = 10$ mHz.

4. Discussion

The space-time samples in Fig. 2, the scatter plots in Fig. 3, the correlation curves in Fig. 4, and the Fourier decompositions in Figs. 5–7 all show that, at the height sampled by our Ca II H images, a brightness pattern exists in quiet-sun internetwork areas which is dominated by subsonic components. The latter have significant partial anticorrelation to the preceding underlying surface granulation. The anticorrelation peaks at 2–3 min time delay and increases with spatial image smoothing (Figs. 2 and 4). Although it remains far from strict 1:1 reversal even at mesogranular resolution, reversed granulation is much more evident at this height than at the heights sampled by the ultraviolet image sequences of Paper I. We estimate these to be about 250 km and 400 km, respectively, rather low compared with the reversal heights reported by Balthasar (1998). Better height determination awaits data with precise Ca II H filter tilt control and numerical response simulation.

What are the nature and the possible roles of reversed granulation? We discuss these by briefly reviewing different options, including some recent literature.

Convection reversal. The solar surface granulation itself is a product of convection reversal. The latter results from radiation losses when convective upwellings pass through optical depth unity, cool radiatively, suffer hydrogen recombination, lose entropy, and are reverted into horizontal outflows coalescing into granular-lane downflows which perform the buoyancy work driving the convection (Stein & Nordlund 1998). Granulation brightness reversal with height results from the radiative cooling of upflow-compressed gas above large granules, splitting them when sinking back, and from radiative heating of sideways flowing gas near and above lanes (Nordlund 1984). This reversal has not been explicitly analysed by Stein and Nordlund in their granulation simulations, nor by Skartlien et al. (2000) in their extension of these with chromospheric wave excitation, but it can be seen in Fig. 10 of Uitenbroek (2000) who used a Stein–Nordlund snapshot to synthesize an infrared CO-line image, and it appears prominently in the recent simulation of solar granulation and wave excitation by Wedemeyer et al. (2004). The latter fails in chromospheric wave energetics through assuming LTE, but is likely correct in predicting reversed-granulation patterns in the middle photosphere. It is of interest to synthesize Ca II H images from such simulations and compare the degree of anticorrelation and time delay with our observed values.

Atmospheric gravity waves. Paper I used TRACE data in a similar analysis to establish that, at the twice-higher formation heights of the 1600 Å and 1700 Å continua, atmospheric gravity waves rather than convection reversal dominate the subsonic internetwork background pattern. In terms of convection theory, convection reversal and gravity wave excitation in the "overshoot layer" are two-of-one-kind phenomena describing the effects of penetration into convectively stable layers. However, in our terms convection reversal describes local effects whereas gravity waves, once excited, propagate slantedly away from their excitation source, interfere constructively or destructively when meeting from different sources, and may reach breaking height unless hitting a low-lying magnetic canopy. Thus, these overshoot phenomena may be very similar in their intrinsic physical nature but differ considerably in topology, effects, and in the brightness patterns they cause.

The large difference in the degree of anticorrelation found here for surface–versus–Ca II H brightness patterns and in Paper I for surface–versus–ultraviolet brightness patterns

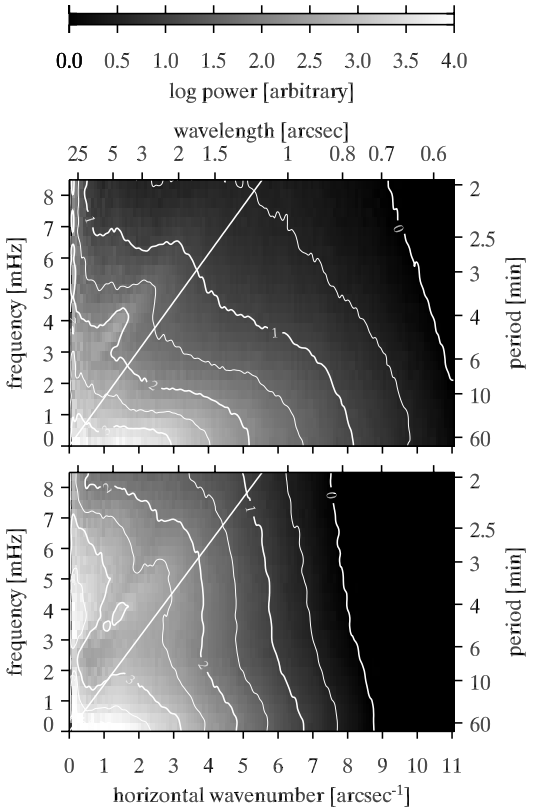

Fig. 6. Two-dimensional brightness power spectra. *Upper panel*: G band. *Lower panel*: Ca II H. Axes: horizontal wavenumber k_h, vertical temporal frequency f. The corresponding wavelengths and periodicities are specified along the top and at right. Grey scale: logarithm of the brightness power after mean and trend removal and smoothing, as coded by the grey-scale bar above the figure and the contours. Slanted line: $f = (1/2\pi)\, c_s\, k_h$ with $c_s = 7$ km s^{-1}.

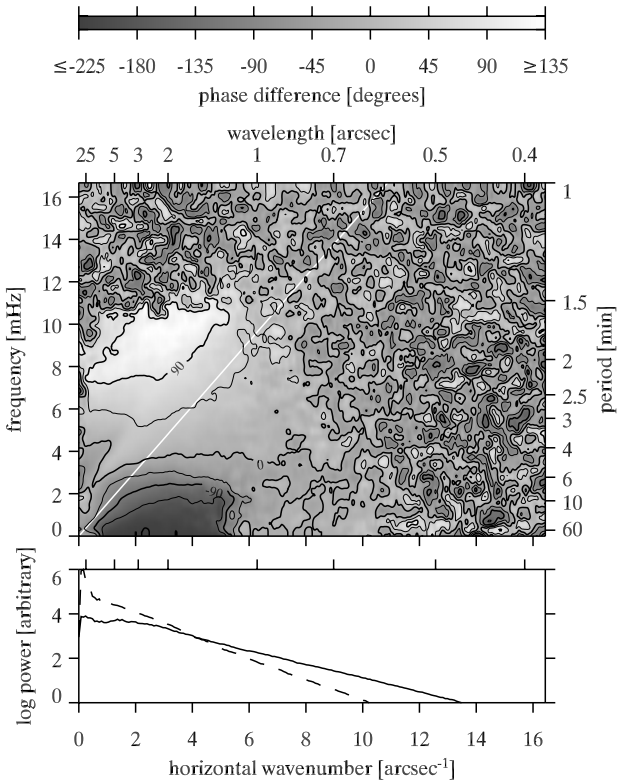

Fig. 7. *Upper panel*: two-dimensional phase difference $\Delta\phi$ (Gb – Ca), in the format of Fig. 6 but with larger axis extents. *Lower panel*: logarithm of the brightness power in the 0–2 mHz frequency band. Solid: G band. Dashed: Ca II H.

indicates that the internetwork background transforms from being mostly set by convection reversal in the low photosphere to being mostly set by gravity wave interference in the high photosphere. The much higher resolution of our Ca II H data does not play a role in this comparison since the upper dashed curve in Fig. 4 shows that the anticorrelation is intrinsically meso-scale at both heights. The fact that the anticorrelation is not largest at granular scales suggests that gravity-wave spreading and interference already contributes significantly to the internetwork background at the Ca II H inner-wing formation height. This is also amenable to comparison with numerical granulation-plus-wave simulations.

Acoustic waves. In a recent paper Cadavid et al. (2003) used a nine-hour dual sequence of G-band and Ca II K filtergrams from the former Swedish Vacuum Solar Telescope in a statistical analysis of joint (or disjoint) occurrence of intergranular darkenings and K-line brightenings. They have since repeated their analysis using our higher-resolution data, and found essentially identical results (private communication), in agreement with the tendency of G-band to Ca II H & K anticorrelations to be clearer at mesogranular scales (Fig. 4). In brief, they find that most intergranular darkenings are followed by K-line brightenings after two minutes and that reversedly most K-line brightenings follow on G-band darkenings, but with small overlap between the two sets. In addition, reversed sequencing (K-line bright before lane darkening) occurs as well. They attribute their findings to a pre-existing, evanescent acoustic wave pattern with four-minute periodicity, and suggest that this pattern is a key part of K_{2V} grain formation in addition to propagative "acoustic-event" wave excitation as studied theoretically by Skartlien et al. (2000) and observationally by Hoekzema et al. (2002).

The second panel of Fig. 6 indeed contains somewhat enhanced Ca II H power at four-minute periodicity and granular scales, which may come from the fundamental mode (cf. Kiefer & Balthasar 1998), but our results indicate that subsonic convection reversal and gravity waves constitute the major grain-making ingredient next to locally-excited three-minute waves. At both the Ca II H and the ultraviolet formation heights, the subsonic contribution contains more power than the sonic contribution and at both heights it is directly observed to contribute substantially to internetwork grain brightness (third columns of Fig. 3 and of Fig. 2 of Paper I). Cram & Damé (1983) already noted that K_{2V} grains are invariably superimposed on a larger-scale brightness pattern. Our work identifies the latter as subsonic, not acoustic, and identifies reversed granulation as a major constituent up to the middle photosphere.

Intergranular magnetism. Two recent papers on intergranular fields are pertinent here. The first is the observational claim by Domínguez Cerdeña et al. (2003) of the existence of small magnetic elements with about 1000 Gauss field strength in as much as one third to half the intergranular lanes in internetwork areas. The other is the magnetoconvection simulation of Schüssler et al. (2003) in which indeed most intergranular lanes contain kiloGauss field concentrations, but only those of about 2000 Gauss show up as G-band bright points in simulated high-resolution images whereas those of about 1000 Gauss do not.

Taking these two papers together implies that also our observed quiet-Sun internetwork areas may be quite full of intergranular kiloGauss fields that do not show up as internetwork "flashers" in our G-band time slices. Since the stronger-field concentrations do show up (Fig. 1) and are noticeably bright in Ca II H & K through an unidentified heating mechanism (just as is the case for network bright points), one might postulate that also 1000 Gauss intergranular fields should cause H & K brightness enhancements, and surmise that our partial correlation between Ca II H brightness and intergranular lanes therefore betrays the presence of intergranular fields not evident in the G band. In other words, that reversed granulation is a proxy for intergranular fields. The partial correlation would then be a measure of how many lanes contain H & K–bright field concentrations, and the increase of correlation with spatial smoothing might come from field spreading with height. Such co-location would also imply support for Sivaraman's persistent stance that K_{2V} grains are mostly magnetic (Sivaraman & Livingston 1982; Sivaraman 1991; Sivaraman et al. 2000). Direct confirmation requires acquiring cospatial high-resolution sequences of very sensitive magnetograms and Ca II H or K filtergrams, correlation analysis as done here, and demonstration that such a correlation does not simply portray field advection in convection reversal without additional heating (cf. Cadavid et al. 2003).

However, we think it unlikely that the observed reversed granulation results from intergranular fields. On the theoretical side, it should be pointed out that the flux density in the simulation of Schüssler et al. (2003) resembles plage or active network rather than quiet internetwork. More in general, such magnetoconvection simulations do not yet include the supergranular flows which sweep actual internetwork areas free of advected fields within a day or so, making it likely that cell interiors contain less field than the simulations.

On the observational side, Fig. 5 of Rutten (2003) indicates that the ultraviolet internetwork background pattern reaches its largest subsonic amplitudes in cell interiors well away from the cell boundaries outlined by network. This is also shown by the bottom panel of Fig. 1 where wide zones of intermediate mean intensity are needed to mask off areas around network where reversed granulation appears less clearly. The subsonic modulation increase towards cell centers suggests that the internetwork background pattern tends to avoid field, rather than mapping it.

Canopy magnetism. Rutten (2003) interpreted the above network avoidance as a mapping of canopy height, on the assumption that gravity waves reach larger brightness amplitude where the canopy is higher. Similar avoidance occurs around active regions, very clearly in a dual Ca II H and G-band active-region mosaic taken with the DOT on June 6, 2003 and available at URL `http://dot.astro.uu.nl`. Blinking the pair shows that the Ca II H internetwork pattern fades away towards the active region already far from the zone of dense G-band-bright field concentrations surrounding the spots. Lighthill (1967, pp. 440–443) has pointed out that gravity waves transform much easier into Alfvén waves along non-vertical magnetic field than acoustic waves. We wonder whether such coupling explains the fading of the subsonic background pattern towards network and active regions, similar to the suppression of acoustic modulation detected by McIntosh & Judge (2001) and Muglach (2003).

5. Conclusion

Using high-quality DOT image sequences sampling the low photosphere in the G band and the middle photosphere in Ca II H, we have quantified the phenomenon of "reversed granulation" as a partial (about 50%) meso-scale correlation between the subsonic brightness components of the Ca II H internetwork pattern and the dark lanes of the surface granulation about 2–3 min earlier. Higher up, this partial anticorrelation weakens further, as shown in the similar analysis in Paper I of ultraviolet images from TRACE.

Multiple options, discussed above, exist to explain the phenomenon. We believe that it primarily represents a mixture of convection reversal and gravity wave excitation with gravity-wave interference gaining dominance at larger heights, and that it has less to do with *p*-mode interference or intergranular magnetism. Numerical simulations appear as the appropriate way to ascertain this balance.

We also think that the phenomenon may be useful as empirical canopy mapper, in studying wave–canopy interactions, and as ingredient in cool-star basal flux interpretation. In any case, the phenomenon adds yet more diagnostic value to the rich list of what may be fruitfully studied using the Ca II H & K lines (cf. introduction to Rutten & Uitenbroek 1991).

Acknowledgements. We are indebted to J. M. Krijger, B. W. Lites, M. P. Rast, H. Uitenbroek and M. Kuperus for discussions. The DOT is operated by Utrecht University at the Spanish Observatorio del Roque de los Muchachos of the Instituto de Astrofísica de Canarias and is presently funded by Utrecht University, The Netherlands Organisation for Scientific Research NWO, The Netherlands Graduate School for Astronomy NOVA, and SOZOU. The DOT efforts are part of the European Solar Magnetism Network. R. J. Rutten acknowledges travel support from the Leids Kerkhoven-Bosscha Fonds, hospitality at the High Altitude Observatory (Boulder), Montana State University (Bozeman) and NSO/Sacramento Peak (Sunspot).

References

Balthasar, H. 1998, Astron. Nachr., 6, 387

Brandt, P. N., Rutten, R. J., Shine, R. A., & Trujillo Bueno, J. 1992, in Cool Stars, Stellar Systems, and the Sun, ed. M. S. Giampapa, & J. A. Bookbinder, ASP Conf. Ser., 26, 161

Brandt, P. N., Rutten, R. J., Shine, R. A., & Trujillo Bueno, J. 1994, in Solar Surface Magnetism, ed. R. J. Rutten, & C. J. Schrijver, NATO ASI Series C 433 (Dordrecht: Kluwer), 251
Cadavid, A. C., Lawrence, J. K., Berger, T. E., & Ruzmaikin, A. 2003, ApJ, 586, 1409
Carlsson, M., & Stein, R. F. 1997, ApJ, 481, 500
Cram, L. E., & Damé, L. 1983, ApJ, 272, 355
Domínguez Cerdeña, I., Sánchez Almeida, J., & Kneer, F. 2003, A&A, 407, 741
Handy, B. N., Acton, L. W., Kankelborg, C. C., et al. 1999, Sol. Phys., 187, 229
Hoekzema, N. M., Rimmele, T. R., & Rutten, R. J. 2002, A&A, 390, 681
Hoekzema, N. M., & Rutten, R. J. 1998, A&A, 329, 725
Kiefer, M., & Balthasar, H. 1998, A&A, 335, L73
Krijger, J. M., Rutten, R. J., Lites, B. W., et al. 2001, A&A, 379, 1052
Lighthill, M. J. 1967, in Aerodynamical Phenomena in Stellar Atmospheres, ed. R. N. Thomas (New York: Academic Press), IAU Symp., 28, 429
Lites, B. W., Rutten, R. J., & Berger, T. E. 1999, ApJ, 517, 1013
McIntosh, S. W., Fleck, B., & Judge, P. G. 2003, A&A, 405, 769
McIntosh, S. W., & Judge, P. G. 2001, ApJ, 561, 420
Muglach, K. 2003, A&A, 401, 685
Nordlund, Å. 1984, in Small-Scale Dynamical Processes in Quiet Stellar Atmospheres, ed. S. L. Keil, National Solar Observatory Summer Conf., Sunspot, 181
Rutten, R. J. 1994, in Chromospheric Dynamics, ed. M. Carlsson, Proc. Miniworkshop, Inst. Theor. Astrophys. Oslo, 25
Rutten, R. J. 2003, in Turbulence, Waves and Instabilities in the Solar Plasma, ed. R. von Fay-Siebenbürgen, K. Petrovay, J.-L. Ballester, & M. Aschwanden, Procs. NATO ARW (Dordrecht: Kluwer), 137
Rutten, R. J., de Pontieu, B., & Lites, B. W. 1999, in High Resolution Solar Physics: Theory, Observations, and Techniques, ed. T. R. Rimmele, K. S. Balasubramaniam, & R. R. Radick, Procs. 19th NSO/Sacramento Peak Summer Workshop, ASP Conf. Ser., 183, 383
Rutten, R. J., Hammerschlag, R. H., Bettonvil, F. C. M., Sütterlin, P., & de Wijn, A. G. 2004, A&A, 413, 1183
Rutten, R. J., & Krijger, J. M. 2003, A&A, 407, 735
Rutten, R. J., & Uitenbroek, H. 1991, Sol. Phys., 134, 15
Schüssler, M., Shelyag, S., Berdyugina, S., Vögler, A., & Solanki, S. K. 2003, ApJ, 597, L173
Sivaraman, K. R. 1991, in Mechanisms of Chromospheric and Coronal Heating, ed. P. Ulmschneider, E. Priest, & B. Rosner (Berlin: Springer Verlag), 44
Sivaraman, K. R., Gupta, S. S., Livingston, W. C., et al. 2000, A&A, 363, 279
Sivaraman, K. R., & Livingston, W. C. 1982, Sol. Phys., 80, 227
Skartlien, R., Stein, R. F., & Nordlund, Å. 2000, ApJ, 541, 468
Stein, R. F., & Nordlund, A. 1998, ApJ, 499, 914
Title, A. M., & Berger, T. E. 1996, ApJ, 463, 797
Uitenbroek, H. 2000, ApJ, 531, 571
Vernazza, J. E., Avrett, E. H., & Loeser, R. 1981, ApJS, 45, 635
Wedemeyer, S., Freytag, B., Steffen, M., Ludwig, H.-G., & Holweger, H. 2004, A&A, 414, 1121